Random Auxetic Porous Materials from Parametric Growth Processes

Jonàs Martínez

Random Auxetic Porous Materials from Parametric Growth Processes

Jonàs Martínez

Université de Lorraine, CNRS, Inria, LORIA
August 4, 2020

Abstract

We introduce a computational approach to optimize random porous materials through parametric growth processes. We focus on the particular problem of minimizing the Poisson's ratio of a two-phase porous random material, which results in an auxetic material. Initially, we perform a parametric optimization of the growth process. Afterward, the optimized growth process is used to directly generate an auxetic random material. Namely, the growth process intrinsically entails the formation of an auxetic material. Our approach enables the computation of large-scale auxetic random materials in commodity computers. We also provide numerical results indicating that the computed auxetic materials have close to isotropic linear elastic behavior.

Introduction

Auxetic structures are materials with negative Poisson's ratio: when stretched they expand perpendicularly to the applied force [1, 2]. Auxetic materials find applications in multiple fields thanks to their excellent shock absorption, fracture toughness, or acoustical and vibrational absorption [3–8] among other reasons. A substantial amount of research is devoted to the design of auxetic mechanical materials [5, 9] that derive their physical properties from the particular arrangement of their small-scale geometry rather than from the material from which they are made. Recent manufacturing technologies can fabricate complex small-scale structures, and therefore manufacture auxetic materials.

Random materials offer some advantages compared to the more widespread periodic materials. In particular, they are more resilient to fabrication related symmetry-breaking imperfections [10], allow to compute the material geometry in an efficient and scalable way [11], and are capable to smoothly and seamlessly grade material properties and conform to any given surface [12]. While most auxetic materials are defined by a repeating periodic structure a distinct line of research is otherwise interested in random auxetic materials [13] since they offer certain advantages over periodic structures [14–16]. Auxetic polymeric foams [2, 17] were reported in the 80s and are widely used in industrial applications. The most common process to obtain auxetic foams consists in compressing a conventional flexible cellular foam to force the cell ribs to buckle, producing a re-entrant structure which is then heated to its softening temperature [18, 19]. The geometry of cellular foams is usually idealized and modeled with Voronoi diagrams [20], and some works studying auxetic foams start by modeling a compressed Voronoi diagram [21, 22]. Alternative methods to produce random auxetic materials consider sheets with random perforations [23] or random fiber networks that can be produced by electrospinning [24].

A recent research direction tackles the minimization of the Poisson's ratio of finite two-dimensional random networks consisting of nodes connected by bonds. Different optimization approaches have been proposed, ideally assuming that the elastic behavior of the network remains isotropic during the iterative optimization process. Reid et al. [25] proposed to iteratively prune network bonds, further improved in [26] by modifying, in addition, the position of the network nodes and the stiffness of the network bonds. Hagh et al. [27] starts from a planar triangulation and iteratively removes bonds while avoiding the creation of reentrant polygons. Liu et al. [28] proposed an iterative adjustment of the bond stiffness. Pashine et al.[29] presented a network aging process that decreases the Poisson's ratio.

We advocate for a different perspective on the problem of computing two-dimensional auxetic random materials that is computationally scalable. We consider a parametric growth process that produces a porous material with a solid and void phase. The growth process is compactly defined by a random point process and two parametric functions controlling the growth law. Our goal is to optimize the parameters of these two functions in order to minimize the Poisson's ratio of the resulting porous material. Importantly, this optimization is only carried out once and allows afterward the immediate generation of random auxetic materials through the process of growth, without requiring any further optimization process. As shown in Figure 1, we enable the computation of large-scale random auxetic porous materials in commodity computers with close to isotropic behavior.

Results

Growth process

We consider a growth process [30] in which nuclei are born at the same time. Each nucleus, a point $x \in \mathbb{R}^2$, is the origin of a cell. Cells evolve according to a growth law and are forbidden to overlap. At the end of the growth, the union of all cells corresponds to the void phase of the porous material, while its complement in $\mathbb{R}^2$ corresponds to the solid phase. We start by describing how the nuclei are placed in space and how the law of growth is defined.

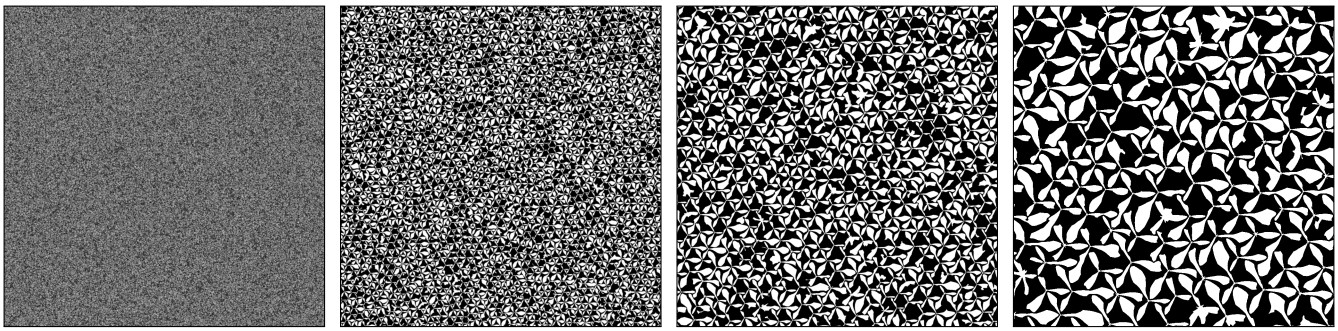

Figure 1: From left to right: large-scale random auxetic porous material with increasing close-up views. The growth process has 43590 nuclei and the computation took 26 minutes on a laptop using a single CPU core.

A two-dimensional point process $\Phi \subset \mathbb{R}^2$ defines the nuclei. We restrict ourselves to two different types of point processes: a homogeneous Poisson point process with intensity $\lambda > 0$, and a hard-core point process in which the points are forbidden to lie closer together than a minimum distance $D > 0$ (e.g. the centers of a jammed packing of disks). In particular, we consider the random sequential adsorption (RSA) model [31], were disks with radius $\frac{D}{2}$ are iteratively added as long as they do not overlap any previously added disk. The center of the disks corresponds to the RSA point process. The point process intensity of this RSA model is $\lambda = \frac{4A}{\pi D^2}$, where $A \approx 0.547$ is the area fraction were saturation occurs [30].

Cells grow through a process of uniform scaling of a compact set $\mathcal{S} \subset \mathbb{R}^2$ centered around each nucleus. The growth ceases whenever and wherever a cell comes into contact with another one (see Figure 2). This type of growth process has been well studied in the literature when $\mathcal{S}$ is a convex set and is also known as the Voronoi growth model [32]. Our central idea is to allow $\mathcal{S}$ to be non-convex, enabling the formation through growth of porous materials with more diverse shapes.

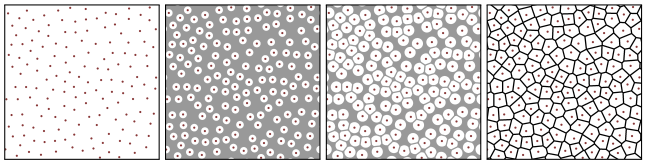

Φ

Figure 2: Given a point process Φ, the cells grow according to the uniform scaling of a Euclidean disk.

In addition, we restrict the growth process with what we call a maximum Euclidean radius of growth (see Figure 3). Let $B_r \subset \mathbb{R}^2$ be a closed Euclidean disk with radius r, and centered at the origin. Let x be a point in the boundary of a growing cell. The growth ceases at x if $x + B_r$ intersects any other growing cell.

We start by giving a precise definition of $\mathcal{S}$. Let $\mathcal{S} \subset \mathbb{R}^2$ be a compact star-shaped set with respect to the origin O. That is, for any point $x \in \mathcal{S}$, the line segment $[x, O]$ is contained in $\mathcal{S}$. The boundary of $\mathcal{S}$ can be parameterized in polar coordinates by a continuous and periodic function $\psi_{\mathcal{S}} : [0, 2\pi] \mapsto [r_{\min}, r_{\max}]$, where $0 < r_{\min} \leq r_{\max}$ are the minimum and maximum Euclidean

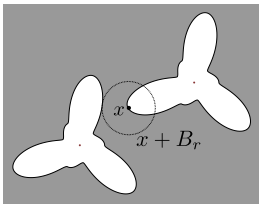

Figure 3: Growth of two cells. The growth ceases at x since the disk $x + B_r$ intersects another growing cell.

distance from O to the boundary of $\mathcal{S}$. A description of the method used to parameterize $\mathcal{S}$ is given in the *Methods* section. The distance induced by $\mathcal{S}$ from a point p to a point x is [33]

$$d_{\mathcal{S}}(p, x) = \frac{\|x - p\|}{\psi_{\mathcal{S}}(\angle(x - p))} , \tag{1}$$

where $\angle(\cdot)$ is the angle of a vector with respect to the horizontal axis, and $\|\cdot\|$ is the Euclidean norm. Intuitively, $d_{\mathcal{S}}(p, x)$ is the factor by which we have to uniformly scale $\mathcal{S}$, centered around p, such that x lies on its boundary. We always consider that p is a cell nucleus and x is any point of the cell emanating from p.

The maximum Euclidean radius of growth is parameterized by a star-shaped set $\mathcal{S}^*$. We consider a polar function $\psi_{\mathcal{S}^*} : [0, 2\pi] \mapsto [r^*_{\min}, r^*_{\max}]$, where $0 < r^*_{\min} \leq r^*_{\max}$ are the minimum and maximum Euclidean radius of growth. Let x be a point in the boundary of a growing cell emanating from $p \in \Phi$. The growth ceases at x if $x + B_{\psi_{\mathcal{S}^*}(\angle(x-p))}$ intersects any other growing cell.

The minimal distance between two points in a Poisson point process can be arbitrarily small. Thus, a cell can be empty as its growth was forbidden through $\mathcal{S}^*$ from the very beginning of the growth process. For a hardcore point process, the minimal distance between two points is at least D and it suffices to enforce $D > r^*_{\max}$ in order to guarantee that all cells are allowed to grow.

It is challenging to formulate a continuous growth law [34] in our setting since both $\mathcal{S}$ and $\mathcal{S}^*$ are not necessarily convex, and $\mathcal{S}^*$ imposes a distinct local constraint on the growth process. We instead resort to a discrete growth process formulation, where the cells grow in discrete steps. Therefore our growth process defines a *discrete random set*. In particular, we consider an integer lattice $L_W = \mathbb{Z}^2 \cap W$ where W is a bounded subset of $\mathbb{R}^2$.

Let $\Phi_W = \Phi \cap W = (p_1, \ldots, p_n)$ be the subset of nuclei in W. The set of lattice points belonging to the cells is given by the union $C_W = \bigcup_{i=1}^{n} C_W^i \subset L_W$, where C_W^i corresponds to the lattice cell points associated with the nuclei p_i. Lattice points are incrementally added to C_W throughout the discrete growth process. Let $S_1 \subset \mathbb{R}^2$ be the unit square centered at the origin, and let $\oplus$ denote the Minkowski sum operator. We consider that the void phase of the porous material is given by $C_W \oplus S_1$, while the solid one is given by $(L_W \setminus C_W) \oplus S_1$. If W is a rectangle, both phases can be compactly represented with a binary digital image. In all illustrations the void phase is colored in white and the solid phase in black. Figures 4 and 5 show an overview of the growth process.

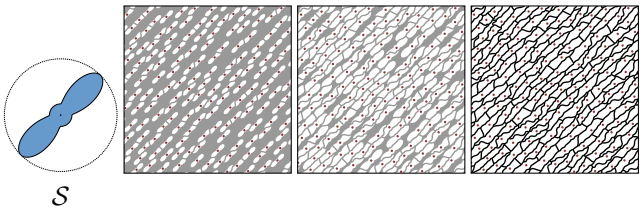

Figure 4: Growth process given by the point process of Figure 2 and the uniform scaling of $\mathcal{S}$ at the left. In this example $\mathcal{S}^*$ is a Euclidean disk.

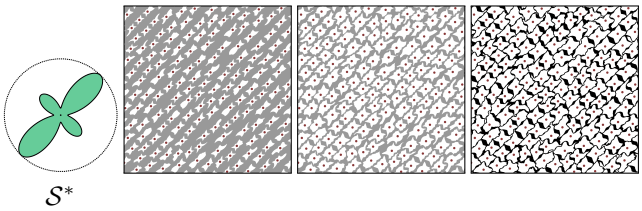

Figure 5: Growth process given by the point process of Figure 2, the uniform scaling of $\mathcal{S}$ in Figure 4, and the maximum Euclidean radius of growth $\mathcal{S}^*$ at the left.

In the following, we describe in more detail Algorithm 1 that simulates the process of discrete growth. An ordered set Q contains tuples $\{x, p\}$ where the first element is a lattice point of $x \in L_W$ and the second one is a nucleus point of $p \in \Phi_W$. Q is ordered according to the distance $d_{\mathcal{S}}(p, x)$ and is used to simulate the discrete growth process over L_W. The tuples in Q identify the points where cell growth can potentially take place. The growth process is divided in two parts, the nucleation phase and the growth phase.

Nucleation Before the growth starts, for all $p_i \in \Phi_W$ we insert in Q the tuple $\{x_i, p_i\}$, where $x_i \in L_W$ is the closest lattice point to p_i. L_W should be sufficiently dense so no two points in Φ_W are closest to the same lattice point in L_W.

Growth The discrete growth process is simulated as follows. Let $\{x, p_i\}$ be the tuple in Q with the smallest distance $d_{\mathcal{S}}(p_i, x)$ among all tuples.

- (Line 8) First, we remove $\{x, p_i\}$ from Q.
- (Lines 9–12) Second, if x does not already belong to any cell and the Euclidean disk $B_{\psi_{\mathcal{S}^*}(\angle(x-p_i))}$ does not contain any other cell point we proceed to add x in C_W^i. That is, the lattice point x now belongs to the cell emanating from p_i.
- (Lines 13–14) Finally, future candidate points of growth around a discrete local neighborhood of p are inserted Q. More precisely, we insert in Q the four tuples $\{x_n, p_i\}$, where x_n is a lattice point in the 4−connected neighborhood of x in L_W.

The above is done iteratively until Q is empty.

Periodic boundary conditions Optionally, when W is a rectangle periodic boundary conditions can be easily imposed by considering that L_W is a periodic lattice as well. If Φ is an RSA point process, the random adsorption of disks has to be performed considering a periodic domain. In this work, periodic boundary conditions are used to generate porous materials that can be simulated with periodic homogenization.

Algorithm 1 discreteGrowthProcess(L_W, Φ_W, $\mathcal{S}$, $\mathcal{S}^*$)

```
1:  C_W^i ← ∅ for all C_W^i ∈ C_W
2:  for p_i ∈ Φ_W do                                   ▷ Nucleation
3:      Let x_i ∈ L_W be the closest lattice point to p_i
4:      Insert in Q the tuple {x_i, p_i}
5:  end for
6:  while Q ≠ ∅ do                                     ▷ Growth
7:      Let {x, p_i} ∈ Q with smallest distance d_S(p_i, x)
8:      Remove {x, p_i} from Q
9:      if x ∉ C_W then
10:         N ← L_W ∩ (x + B_{ψ_{S*}(∠(x−p_i))})
11:         if (y ∉ C_W) ∨ (y ∈ C_W^i) for all y ∈ N then
12:             C_W^i ← C_W^i ∪ {x}
13:             for x_n ∈ neighborhood of x in L_W do
14:                 if x_n ∉ C_W then
15:                     Insert in Q the tuple {x_n, p_i}
16:                 end if
17:             end for
18:         end if
19:     end if
20: end while
```

Cell regularization In our discrete setting, connectedness is given for the lattice L_W with respect to a 4-connected neighborhood. Algorithm 1 is guaranteed to produce discrete cells C_W^i that are connected sets. However, when $\mathcal{S}^*$ is not convex it may occur that a cell has a genus higher than zero (i.e. has "holes"). This leads to a porous material solid phase composed of more than one connected component, which is undesirable. To resolve this we fill any hole that a cell may have. Formally, we consider the complement of the unbounded component of the complement of a cell (see Figure 6). We denominate this last step *cell regularization*

Stochastic homogenization

We study the elastic behavior of the random porous materials given by our growth process. We restrict our analysis to linear elasticity which is useful to model the

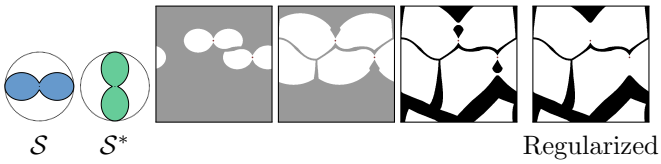

Figure 6: Left: $\mathcal{S}$ and $\mathcal{S}^*$ governing the growth process of two nuclei. Middle: evolution of the growth, the holes arise due to the high anisotropy of both $\mathcal{S}$ and $\mathcal{S}^*$, and the particular arrangement of the two nuclei. Right: the two cell holes are simply filled.

behavior of materials under small deformations. In particular, we consider the stochastic homogenization [35] of the random porous material in order to derive its average linear elastic constitutive behavior.

Hooke's law represents the material behavior of elastic materials with the linear relation $\sigma = C\epsilon$, where σ is the stress, ϵ is the strain, and C is the elasticity tensor (a symmetric and positive definite matrix), in Voigt notation [36]

$$\begin{bmatrix} \sigma_1 \\ \sigma_2 \\ \sigma_{12} \end{bmatrix} = \begin{bmatrix} c_{11} & c_{12} & c_{13} \\ c_{12} & c_{22} & c_{23} \\ c_{13} & c_{23} & c_{33} \end{bmatrix} \begin{bmatrix} \epsilon_1 \\ \epsilon_2 \\ 2\epsilon_{12} \end{bmatrix} \tag{2}$$

Periodic homogenization [37] seeks to find the elasticity tensor characterizing a periodic composite material defined from a periodic cell, as the length of the cell tends to zero. In the periodic case, the homogenization is defined on a finite domain (periodic cell) while on the random case is defined on the whole space $\mathbb{R}^2$, and cannot be reduced to a problem posed on a finite domain [38].

We approximate the homogenized elasticity tensor coefficients of a random porous material, by means of the so called "cut-off" techniques. Consider a periodized cut $[0, s]^2$ (a square) of a stationary random material and its corresponding homogenized elasticity tensor C^s. It was shown in [38] that $\lim_{s\to\infty} C^s$ converges, almost surely. Nevertheless, s needs to be bounded for practical purposes of computation.

In our discrete setting, s is a positive integer value that corresponds to the pixel resolution $s \times s$ of the porous material image. In all results, we consider a constant $D = 80$ for the RSA point process, and $\lambda = \frac{4A}{\pi D^2} \approx 0.000\,11$ for the Poisson point process. Therefore, both tested point processes have similar intensity.

Let $\mathbb{E}[\cdot]$ be the expectation of a random variable. We estimate the value of $\mathbb{E}[C^s]$ with the average of k independent realizations of the random porous material giving $(C^s)_i$, $1 < i \leq k$

$$\mathbb{E}[C^s] \approx \overline{C^s} = \frac{1}{k} \sum_{i=1}^{k} (C^s)_i \tag{3}$$

This is an approximation (Monte Carlo method) frequently used in the context of stochastic homogenization [35]. Let $std(C^s)$ be the standard deviation of the k independent realizations $(C^s)_i$. A range of plausible values for $\mathbb{E}[C^s]$ is $\left(\overline{C^s} \pm 1.96 \frac{std(C^s)}{\sqrt{k}}\right)$ for a confidence interval with probability 95% (see Figure 7).

In order the evaluate the accuracy of the stochastic homogenization [39] we examine the statistical fluctuations of the material porosity $p \in [0, 1]$ (the area fraction of the void phase) for a given k and s. In particular, we consider the coefficient of variation $c_v(p) = \frac{std(p)}{\overline{p}}$ that indicates the extent of variability of the porosity in relation to the mean. Increasing the value of k and s most likely decreases $c_v(p)$. Following [40] we consider that the approximation is sufficiently precise if $c_v(p)$ is below a maximum predefined one. In all the following results we always consider $k = 60$ realizations.

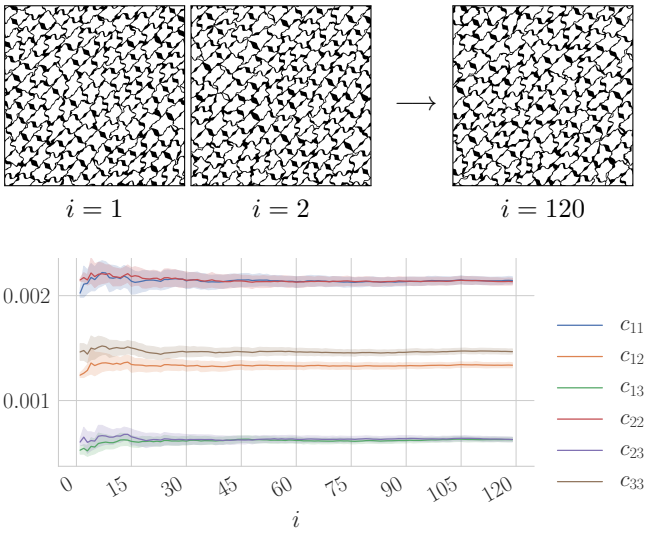

Figure 7: Approximation of the elasticity tensor of the random porous material of Figure 5 in a square with size $s = 1200$, and a total of 120 independent realizations. Left: Some realizations. Right: mean and confidence interval of each tensor component. As the number of realizations i increases, the mean stabilizes and the confidence interval becomes narrower. The coefficient of variation of porosity is $c_v(p) = 0.004\,09$.

Isotropic elasticity

Since our goal is to minimize the Poisson's coefficient of an isotropic material, we give here a brief presentation of how we approximate the isotropic elastic behavior of a random material elasticity tensor, given its average elasticity tensor $\overline{C^s}$.

An isotropic material has an elasticity tensor C^{iso} with only two independent components c_{12}^{iso} and c_{12}^{iso}

$$C^{iso} = \begin{bmatrix} c_{11}^{iso} & c_{12}^{iso} & 0 \\ c_{12}^{iso} & c_{11}^{iso} & 0 \\ 0 & 0 & \frac{c_{11}^{iso} - c_{12}^{iso}}{2} \end{bmatrix} \tag{4}$$

The relation between the tensor components $c_{11}^{iso}, c_{12}^{iso}$ and the Young's moduli $E > 0$ and the Poisson's ratio $v \in [-1, 1]$ is given by

$$E = \frac{(c_{11}^{iso})^2 - (c_{12}^{iso})^2}{c_{11}^{iso}} \qquad v = \frac{c_{12}^{iso}}{c_{11}^{iso}} \tag{5}$$

In practice, it seldomly occurs that an elasticity tensor $\overline{C^s}$ is perfectly isotropic. Thus, we seek to determine its closest isotropic tensor [41]. We consider the standard Frobenius norm for a 3×3 matrix A

$$\|A\|_F = \sqrt{\sum_{i=1}^{3}\sum_{j=1}^{3} |a_{ij}|^2} \tag{6}$$

and minimize the Frobenius norm between C^{iso} and the average tensor $\overline{C^s}$

$$\min_{c_{11}^{iso}, c_{12}^{iso}} \left\| \overline{C^s} - C^{iso} \right\|_F \tag{7}$$

We provide in the *Methods* section the closed-form expression of $c_{11}^{iso}, c_{12}^{iso}$ minimizing Equation (7).

We also need a measure of the deviation of $\overline{C^s}$ from perfect isotropy. We consider the typically used normalized measure δ_{iso} [15, 42]

$$\delta_{iso} = \frac{\left\| \overline{C^s} - C^{iso} \right\|_F}{\left\| \overline{C^s} \right\|_F} \geq 0 \tag{8}$$

where $\delta_{iso} = 0$ indicates perfect isotropy, and increasing values indicate divergence from isotropy.

It is known that periodic structures in $\mathbb{R}^2$ having three-fold rotational symmetry (invariant to rotations of $\frac{2\pi}{3}$) lead to an isotropic linear elastic behavior [43]. We hypothesize that a resembling property holds in our instance of random growth.

A two-dimensional point process Φ is *stationary* if $\Phi + x$ has the same probability distribution than Φ, for all $x \in \mathbb{R}^2$. Φ is *isotropic* if $R(a)\Phi$ has the same probability distribution than Φ, for all rotations $R(a)$ of angle $a \in \mathbb{R}$ around the origin. Both the Poisson point process and the RSA point process are stationary and isotropic point processes [30, 44]. The notion of stationarity and isotropy extends to general random sets.

Let us consider a rotation of $R(\frac{2\pi}{3}n)$, for $n \in \mathbb{Z}$. The probability distribution of Φ is invariant to a rotation $R(\frac{2\pi}{3}n)$. Moreover, if $\mathcal{S}$ and $\mathcal{S}^*$ are three-fold symmetric then $R(\frac{2\pi}{3}n)\mathcal{S} = \mathcal{S}$ (same for $\mathcal{S}^*$). Given a point $p \in \Phi$ then we have

$$R(\frac{2\pi}{3}n)(p+\mathcal{S}) = R(\frac{2\pi}{3}n)p + R(\frac{2\pi}{3}n)\mathcal{S} = R(\frac{2\pi}{3}n)p + \mathcal{S} \tag{9}$$

i.e., the rotation of $\mathcal{S}$ centered at p around the origin keeps $\mathcal{S}$ and $\mathcal{S}^*$ invariant. We infer that the growth process is stationary and invariant to rotations $R(\frac{2\pi}{3}n)$ which leads us to the following hypothesis.

Hypothesis 1. *Let Φ be a stationary and isotropic point process. Let $\mathcal{S}$ and $\mathcal{S}^*$ be three-fold rotational symmetric. For $s \to \infty$ the discrete growth process described in this article gives a porous material with δ_{iso} close to zero. That is, the resulting porous material has close to isotropic linear elastic behavior.*

We have numerically evaluated Hypothesis 1 for a large set of porous materials with different sets $\mathcal{S}$ and $\mathcal{S}^*$, and increasing size s (see Figure 8). There is strong evidence that as s increases the average value of δ_{iso} decreases and it appears to tend towards a value close to zero.

In all the subsequent optimization results considering three-fold rotational symmetric sets $\mathcal{S}$ and $\mathcal{S}^*$ we consider a fixed square size of $s = 1200$. This size gave among all the tests performed in Figure 8 a maximum coefficient of variation of porosity of $c_v(p) = 0.035\,19$ for the Poisson point process, and of $c_v(p) = 0.011\,18$ for the RSA point process.

We also evaluate the impact of the cell regularization over the porosity. More precisely, we measure the relative amount of cell holes that are filled during the cell regularization. Let $\hat{p}$ be the porosity of the porous material before performing the cell regularization. We consider the relative measure $\zeta_{p,\hat{p}} = \left| \frac{\hat{p}-p}{\hat{p}} \right| \geq 0$. For all the results in Figure 8 the maximum value of $\zeta_{p,\hat{p}}$ is $0.061\,57$ and the mean is $0.004\,33$ for the Poisson point process, and maximum $0.019\,48$ and mean $0.000\,41$ for the RSA point process. This indicates that the effect of the cell regularization on the porosity is almost negligible, and is particularly small for the RSA point process.

Parametric optimization

By this point, we have all the ingredients to formulate the parametric optimization of the growth process. Let $\overline{C^s}(\psi_{\mathcal{S}}, \psi_{\mathcal{S}^*})$ be the average elasticity tensor of a porous material parameterized by the functions $\psi_{\mathcal{S}}$ (star-shaped distance) and $\psi_{\mathcal{S}^*}$ (maximum Euclidean radius of growth). Let $\mathbb{F} : M \mapsto \mathbb{R}$ be the objective function, where M is a 3×3 symmetric matrix. Our objective is to minimize

$$\arg\min_{\psi_{\mathcal{S}}, \psi_{\mathcal{S}^*}} \mathbb{F}(\overline{C^s}(\psi_{\mathcal{S}}, \psi_{\mathcal{S}^*})) = \frac{c_{12}^{iso}}{c_{11}^{iso}} \tag{10}$$

where $c_{11}^{iso}, c_{12}^{iso}$ are derived from $\overline{C^s}(\psi_{\mathcal{S}}, \psi_{\mathcal{S}^*})$ considering Equation (15). In order to obtain a physical behavior close to isotropic elasticity we constrain $\mathcal{S}$ and $\mathcal{S}^*$ to be three-fold rotational symmetric. More details of particular choice of optimization method are given in the *Methods* section.

Figures 9 to 11 provide minimization results of the Poisson's ratio with an increasing optimization domain of $\psi_{\mathcal{S}^*}$, and a constant optimization domain of $\psi_{\mathcal{S}} \in [0.05, 1.0]$.

Discussion

We have presented a novel computational approach based on parametric growth processes to minimize the Poisson's ratio of random porous materials. The results attain a negative Poisson's ratio while providing a careful numerical analysis showing close to isotropic behavior. We observe that increasing the number of parameters of $\psi_{\mathcal{S}}$ and $\psi_{\mathcal{S}^*}$ and their domain further improves the minimization. We recommend the use of a hardcore

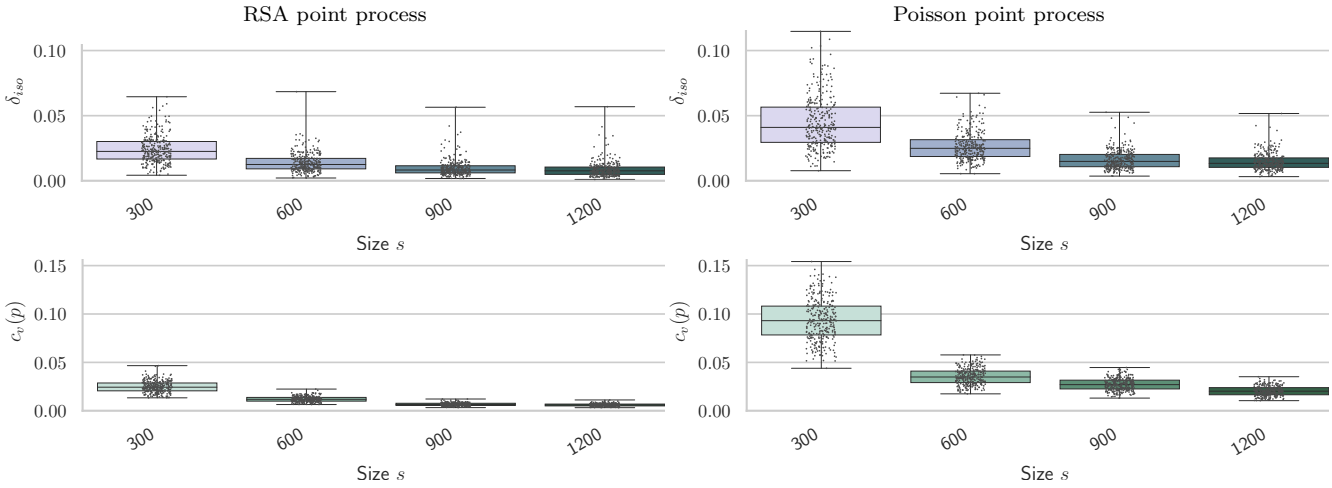

Figure 8: Analysis of the deviation of isotropy δ_{iso} and coefficient of variation of the porosity $c_v(p)$ for a large number of porous materials, and two different point processes (left and right columns). $\mathcal{S}$ and $\mathcal{S}^*$ are three-fold rotational symmetric. The colored boxes encompass the interquartile range of values of δ_{iso}. We consider 4 different sizes s, going from 300 to 1200 For each point process and size we enumerate 300 different random radial spans in the range $\psi_{\mathcal{S}} \in [0.05, 1.0]$ and $\psi_{\mathcal{S}^*} \in [4.0, 40.0]$, and 8 different equally spaced angles in $[0, \frac{2\pi}{3}]$ (three-fold symmetry) considering a total of $2 \cdot 4 \cdot 300 = 2400$ different porous materials. In general, we observe a clear trend of the average value of δ_{iso} and $c_v(p)$ getting closer to zero as the size s of the domain increases. We also notice lower average values with the RSA point process compared to the Poisson point process.

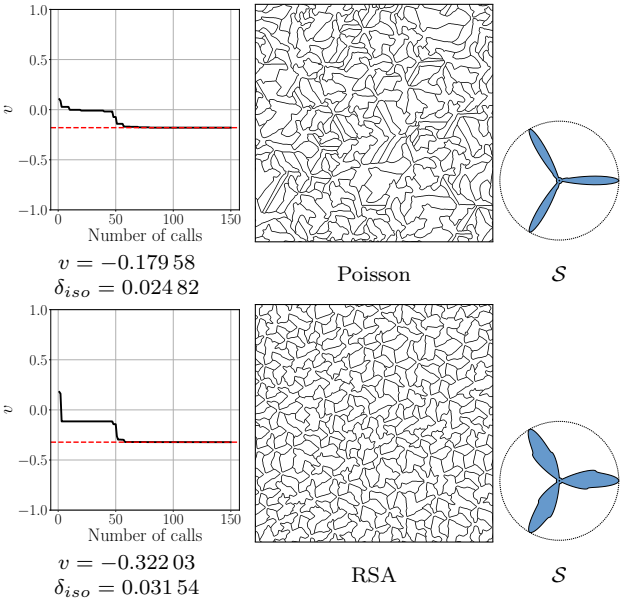

Figure 9: Optimization with constant $\psi_{\mathcal{S}^*} = 4.0$.

point process instead of a Poisson point process to reach lower Poisson's ratio and lower variance of the material properties in a finite extent (see Figure 8).

We distinguish two clear trends from the optimization results. First, the RSA point process is able to achieve lower Poisson's ratio v compared to the Poisson point process. Second, increasing the domain of function $\psi_{\mathcal{S}^*}$ leads to lower Poisson's ratio, since we expand the space of achievable porous materials.

With a parametric growth process, it is possible to generate heterogeneous materials by simply considering that both funcitions $\psi_{\mathcal{S}}$ and $\psi_{\mathcal{S}^*}$ are varying in the space (see Figure 2). One of the main advantages of our approach over periodic structures is that the transitions between different material properties do not need to be handled [45], as they are intrinsically captured by parameters governing the growth process.

Our approach also opens up different opportunities for future work. For instance, to extend it to the 3D case by considering a 3D growth process and adapting the parameterization of $\mathcal{S}$ and $\mathcal{S}^*$. This may be of interest for the inverse design of random 3D porous materials, e.g. random foams are of interest for acoustic absorption [46] or tissue engineering [47]. Moreover, our approach may open the door to other applications besides the minimization of the Poisson's ratio of linearly elastic materials. For example, to tackle the inverse design and optimization of porous materials [12, 48] using our growth process. In most cases, it is sufficient to replace the objective function of Equation (10) with another one of interest.

Methods

Parameterization of the star-shaped set $\mathcal{S}$ Following [33] we parameterize $\mathcal{S}$ with a few known values $(\alpha_i, l_i)_{i>0}$ of the function $\psi_{\mathcal{S}}(\alpha_i) = l_i$, and we call them *radial spans*. For simplicity we always consider $m > 0$ equally spaced radial spans separated by an angle of $\alpha_m = \frac{m}{2\pi}$, and starting at an angle of zero $\alpha_1 = 0$. Let $\alpha_{jk} \in [0, 2\pi]$ be an angle that we seek to interpolate, lying between (α_j, l_j) and (α_k, l_k), such that $k = \lfloor \alpha_{jk} \alpha_m \rfloor$ and $j = (k+1) \mod m$. The relative position t of α_{jk} between α_k $(t = 0)$ and α_j $(t = 1)$ is given by the fractional part $t = \alpha_{jk}\alpha_m - \lfloor \alpha_{jk}\alpha_m \rfloor \in [0, 1)$. Then, we interpolate the value of $\psi_{\mathcal{S}}(\alpha_{jk})$ by considering the following cubic Hermite spline on the unit interval

$$\psi_{\mathcal{S}}(\alpha_{jk}) = (2t^3 - 3t^2 + 1)l_k + (-2t^3 + 3t^2)l_j \qquad (11)$$

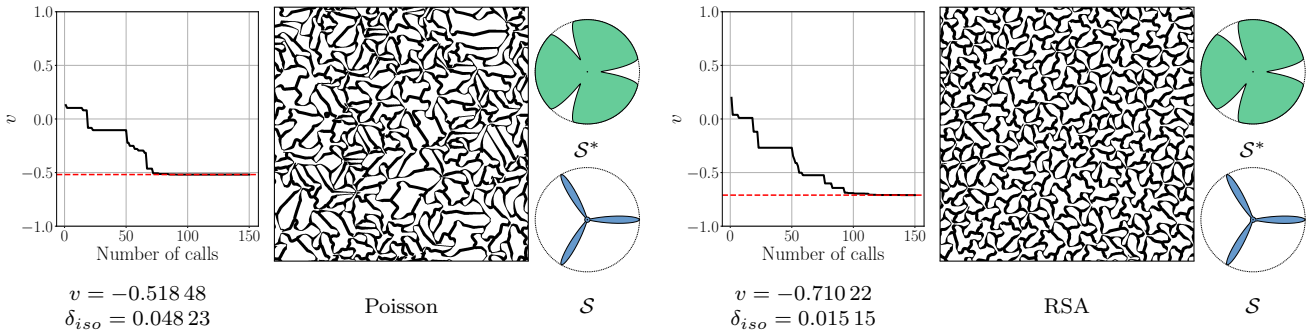

Figure 10: Optimization with variable $\psi_{\mathcal{S}^*} \in [4.0, 15.0]$

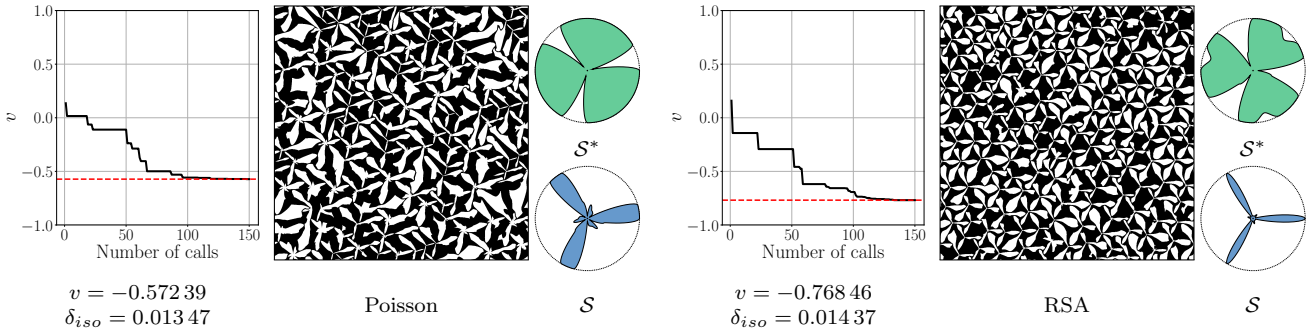

Figure 11: Optimization with variable $\psi_{\mathcal{S}^*} \in [4.0, 40.0]$

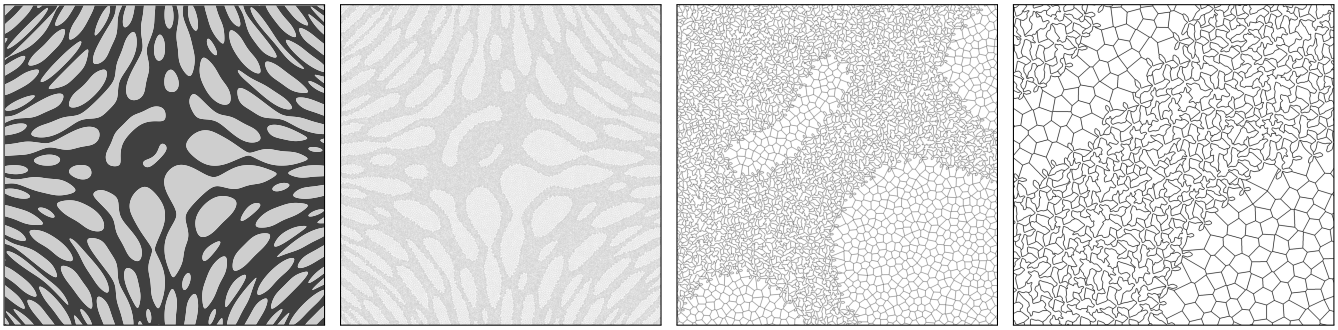

Figure 12: Spatially varying growth process with two different growth functions. Left: Input heterogeneous field, the darker regions correspond to the optimized $\psi_{\mathcal{S}}$ in Figure 9, while the rest correspond to a growth according to the Euclidean disk.

The above interpolation ensures that $\psi_{\mathcal{S}}(\alpha_{jk})$ lies in between l_k and l_j by setting the starting and ending tangents of the spline to zero. In addition, we can easily impose rotational symmetries to the interpolation. An illustration of the interpolation procedure is shown in Figure 13.

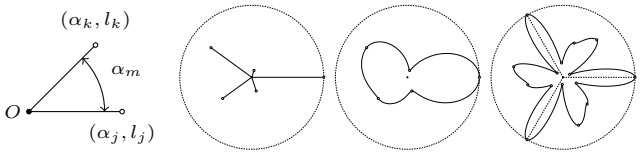

Figure 13: Star-shaped set parameterization. Five equally spaced radial spans and the interpolation result. Left: imposing three-fold rotational symmetry.

Numerical homogenization We compute the homogenized elasticity tensor C^s with a publicly available numerical homogenization method based on the finite element method [49]. The input is an image with values identifying each distinct phase of the periodic material. We impose periodic boundary conditions on the growth process in order to produce a suitable input image. The solid phase is composed of a linear elastic isotropic material with unit Young's modulus $E = 1.0$ and Poisson's ratio $v = 0.3$.

Parametric optimization method The input of function $\mathbb{F}$ is expensive to evaluate, has no closed form, and it involves a numerical Montecarlo approximation. In this case, Bayesian optimization [50] is often a good choice to tackle the optimization. In particular, we have used Bayesian optimization using Gaussian processes as implemented in the Python library *scikit-optimize* [51]. Both functions $\psi_{\mathcal{S}}$ and $\psi_{\mathcal{S}^*}$ are parameterized with $m = 8$ radial spans. We set the first radial span of $\psi_{\mathcal{S}}$ to a constant value of 1, removing an unnecessary degree of freedom. For the Bayesian optimization, we set a maximum number of 150 evaluations of function $\mathbb{F}$, and 50 random initial guesses.

Derivation of c_{11}^{iso} and c_{12}^{iso} For the three-dimensional case, the minimizing values of $c_{11}^{iso}, c_{12}^{iso}$ were derived, for instance, in [52]. We were not able to find any previous work concerning the simpler two-dimensional case. Nevertheless, the values minimizing Equation (7) can be derived by simple calculus. Consider the function f with two arguments c_{11}^{iso} and c_{12}^{iso}

$$\begin{aligned} f &= \left\| C - C^{iso} \right\|_F^2 \\ &= (c_{11} - c_{11}^{iso})^2 + 2(c_{12} - c_{12}^{iso})^2 + (c_{22} - c_{11}^{iso})^2 \\ &\quad + 2c_{13}^2 + 2c_{23}^2 + \left(c_{33} - \frac{c_{11}^{iso} - c_{12}^{iso}}{2} \right)^2 \end{aligned} \tag{12}$$

whose first-order partial derivatives are

$$\begin{aligned} \frac{\partial f}{\partial c_{11}^{iso}} &= -c_{33} - 2(c_{22} - c_{11}^{iso}) + \frac{c_{11}^{iso} - c_{12}^{iso}}{2} - 2(c_{11} - c_{11}^{iso}) \\ \frac{\partial f}{\partial c_{12}^{iso}} &= c_{33} - 4(c_{12} - c_{12}^{iso}) - \frac{c_{11}^{iso} - c_{12}^{iso}}{2} \end{aligned} \tag{13}$$

The Hessian matrix H of f

$$H = \begin{bmatrix} \frac{\partial^2 f}{\partial (c_{11}^{iso})^2} & \frac{\partial^2 f}{\partial c_{11}^{iso} c_{12}^{iso}} \\ \frac{\partial^2 f}{\partial c_{12}^{iso} c_{11}^{iso}} & \frac{\partial^2 f}{\partial (c_{12}^{iso})^2} \end{bmatrix} = \begin{bmatrix} \frac{9}{2} & -\frac{1}{2} \\ -\frac{1}{2} & \frac{9}{2} \end{bmatrix} \tag{14}$$

is positive definite everywhere and it follows that f is a convex function. Since $\frac{\partial^2 f}{\partial (c_{11}^{iso})^2} = \frac{\partial^2 f}{\partial (c_{12}^{iso})^2} > 0$ the function f has a global minimum at

$$\begin{aligned} c_{11}^{iso} &= \frac{1}{20}(9(c_{11} + c_{22}) + 2c_{12} + 4c_{33}) \\ c_{12}^{iso} &= \frac{1}{20}(c_{11} + c_{22} + 18c_{12} - 4c_{33}) \end{aligned} \tag{15}$$

found by solving the system of linear equations from Equation (13) being equal to zero.

Code availability

An open source implementation of our approach can be found at `https:\\future-url-code`. We provide an script to automate the generation of all paper results and figures, apart from the manually done Figure 3.

Data availability

All the results of this article can be downloaded from `https:\\future-url-data`.

Acknowledgments

This work was partly supported by ANR MuFFin (ANR-17-CE10-0002).

References

1. Kolpakov, A. "Determination of the average characteristics of elastic frameworks". *J. Appl. Math. Mech.* **49,** 739–745 (1985).
2. Lakes, R. "Foam structures with a negative Poisson's ratio". *Science* **235,** 1038–1041 (1987).
3. Yang, W., Li, Z.-M., Shi, W., Xie, B.-H. & Yang, M.-B. "Review on auxetic materials". *Journal of materials science* **39,** 3269–3279 (2004).
4. Saxena, K. K., Das, R. & Calius, E. P. "Three decades of auxetics research – materials with negative Poisson's ratio: a review". *Advanced Engineering Materials* **18,** 1847–1870 (2016).
5. Kolken, H. M. & Zadpoor, A. "Auxetic mechanical metamaterials". *RSC Advances* **7,** 5111–5129 (2017).
6. Lakes, R. S. "Negative-Poisson's-ratio materials: auxetic solids". *Annual review of materials research* **47,** 63–81 (2017).
7. Ren, X., Das, R., Tran, P., Ngo, T. D. & Xie, Y. M. "Auxetic metamaterials and structures: A review". *Smart materials and structures* **27,** 023001 (2018).
8. Qin, G. & Qin, Z. "Negative Poisson's ratio in two-dimensional honeycomb structures". *npj Computational Materials* **6,** 1–6 (2020).
9. Dagdelen, J., Montoya, J., de Jong, M. & Persson, K. "Computational prediction of new auxetic materials". *Nature communications* **8,** 1–8 (2017).
10. Portela, C. M. *et al.* "Extreme mechanical resilience of self-assembled nanolabyrinthine materials". *Proceedings of the National Academy of Sciences* **117,** 5686–5693 (2020).
11. Martínez, J., Dumas, J. & Lefebvre, S. "Procedural Voronoi Foams for Additive Manufacturing". *ACM Transactions on graphics* **35,** 44:1–44:12 (2016).
12. Siddhant, K., Tan, S., Li, Z. & Kochmann, D. M. "Inverse-designed spinodoid metamaterials". *npj Computational Materials* **6** (2020).
13. Mirzaali, M., Pahlavani, H. & Zadpoor, A. "Auxeticity and stiffness of random networks: Lessons for the rational design of 3D printed mechanical metamaterials". *Applied Physics Letters* **115,** 021901 (2019).
14. Rayneau-Kirkhope, D., Bonfanti, S. & Zapperi, S. "Density scaling in the mechanics of a disordered mechanical meta-material". *Applied Physics Letters* **114,** 111902 (2019).
15. Zerhouni, O., Tarantino, M. & Danas, K. "Numerically-aided 3D printed random isotropic porous materials approaching the Hashin-Shtrikman bounds". *Composites Part B: Engineering* **156,** 344–354 (2019).
16. Krishnaswamy, J. A., Buroni, F. C., Melnik, R., Rodriguez-Tembleque, L. & Saez, A. "Design of polymeric auxetic matrices for improved mechanical coupling in lead-free piezocomposites". *Smart Materials and Structures* **29,** 054002 (2020).
17. Caddock, B. & Evans, K. "Microporous materials with negative Poisson's ratios. I. Microstructure and mechanical properties". *Journal of Physics D: Applied Physics* **22,** 1877 (1989).

18. Chan, N. & Evans, K. "Fabrication methods for auxetic foams". *Journal of materials Science* **32,** 5945–5953 (1997).
19. Alderson, K., Alderson, A., Ravirala, N., Simkins, V. & Davies, P. "Manufacture and characterisation of thin flat and curved auxetic foam sheets". *physica status solidi (b)* **249,** 1315–1321 (2012).
20. Gibson, L. J. & Ashby, M. F. *Cellular solids: structure and properties* (Cambridge university press, 1999).
21. Li, D., Dong, L., Yin, J. & Lakes, R. S. "Negative Poisson's ratio in 2D Voronoi cellular solids by biaxial compression: a numerical study". *Journal of materials science* **51,** 7029–7037 (2016).
22. Gao, R., Li, D., Dong, L. & Wang, X. "Numerical Analysis of the Mechanical Properties of 3D Random Voronoi Structures With Negative Poisson's Ratio". *physica status solidi (b),* 1800539 (2019).
23. Grima, J. N., Mizzi, L., Azzopardi, K. M. & Gatt, R. "Auxetic perforated mechanical metamaterials with randomly oriented cuts". *Advanced materials* **28,** 385–389 (2016).
24. Domaschke, S., Morel, A., Fortunato, G. & Ehret, A. "Random auxetics from buckling fibre networks". *Nature communications* **10,** 1–8 (2019).
25. Reid, D. R. *et al.* "Auxetic metamaterials from disordered networks". *Proceedings of the National Academy of Sciences* **115,** 1384–1390 (2018).
26. Reid, D. R., Pashine, N., Bowen, A. S., Nagel, S. R. & de Pablo, J. J. "Ideal isotropic auxetic networks from random networks". *Soft Matter* **15,** 8084–8091 (2019).
27. Hagh, V. F. & Thorpe, M. "Disordered auxetic networks with no reentrant polygons". *Physical Review B* **98,** 100101 (2018).
28. Liu, J., Nie, Y., Tong, H. & Xu, N. "Realizing negative Poisson's ratio in spring networks with close-packed lattice geometries". *Physical Review Materials* **3,** 055607 (2019).
29. Pashine, N., Hexner, D., Liu, A. J. & Nagel, S. R. "Directed aging, memory, and nature's greed". *Science advances* **5** (2019).
30. Chiu, S. N., Stoyan, D., Kendall, W. S. & Mecke, J. *Stochastic geometry and its applications* (John Wiley & Sons, 2013).
31. Widom, B. "Random sequential addition of hard spheres to a volume". *The Journal of Chemical Physics* **44,** 3888–3894 (1966).
32. Okabe, A., Boots, B., Sugihara, K. & Chiu, S. N. *Spatial tessellations: concepts and applications of Voronoi diagrams* (John Wiley & Sons, 2000).
33. Martínez, J. *et al.* "Star-Shaped Metrics for Mechanical Metamaterial Design". *ACM Transactions on Graphics* **38,** 1–13 (2019).
34. Aletti, G., Bongiorno, E. G. & Capasso, V. "Integration in a dynamical stochastic geometric framework". *ESAIM: Probability and Statistics* **15,** 402–416 (2011).
35. Blanc, X., Le Bris, C. & Legoll, F. "Some variance reduction methods for numerical stochastic homogenization". *Philos. T. R. Soc. A* **374,** 20150168 (2016).
36. Voigt, W. *Lehrbuch der kristallphysik* (Teubner Leipzig, 1928).
37. Allaire, G. "Homogenization and two-scale convergence". *SIAM Journal on Mathematical Analysis* **23,** 1482–1518 (1992).
38. Bourgeat, A. & Piatnitski, A. "Approximations of effective coefficients in stochastic homogenization". *Annales de l'IHP Probabilités et statistiques* **40,** 153–165 (2004).
39. Kanit, T., Forest, S., Galliet, I., Mounoury, V. & Jeulin, D. "Determination of the size of the representative volume element for random composites: statistical and numerical approach". *Int. J. Solids Struct.* **40,** 3647–3679 (2003).
40. Stroeven, M., Askes, H. & Sluys, L. "Numerical determination of representative volumes for granular materials". *Computer Methods in Applied Mechanics and Engineering* **193,** 3221–3238 (2004).
41. Moakher, M. & Norris, A. N. "The closest elastic tensor of arbitrary symmetry to an elasticity tensor of lower symmetry". *Journal of Elasticity* **85,** 215–263 (2006).
42. Tran, V., Guilleminot, J., Brisard, S. & Sab, K. "Stochastic modeling of mesoscopic elasticity random field". *Mechanics of Materials* **93,** 1–12 (2016).
43. Forte, S. & Vianello, M. "Symmetry classes for elasticity tensors". *Journal of Elasticity* **43,** 81–108 (1996).
44. Stoyan, D. & Schlather, M. "Random sequential adsorption: relationship to dead leaves and characterization of variability". *Journal of Statistical Physics* **100,** 969–979 (2000).
45. Garner, E., Kolken, H. M., Wang, C. C., Zadpoor, A. A. & Wu, J. "Compatibility in microstructural optimization for additive manufacturing". *Additive Manufacturing* **26,** 65–75 (2019).
46. Han, F., Seiffert, G., Zhao, Y. & Gibbs, B. "Acoustic absorption behaviour of an open-celled aluminium foam". *Journal of Physics D: Applied Physics* **36,** 294 (2003).
47. Lanza, R., Langer, R., Vacanti, J. P. & Atala, A. *Principles of tissue engineering* (Academic press, 2020).
48. Ronellenfitsch, H., Stoop, N., Yu, J., Forrow, A. & Dunkel, J. "Inverse design of discrete mechanical metamaterials". *Physical Review Materials* **3,** 095201 (9 2019).
49. Andreassen, E. & Andreasen, C. S. "How to determine composite material properties using numerical homogenization". *Computational Materials Science* **83,** 488–495 (2014).
50. Močkus, J. *On Bayesian methods for seeking the extremum.* in *Optimization techniques IFIP technical conference* (1975), 400–404.
51. Tim, H., Gilles, L. & Iaroslav, S. *scikit-optimize 0.7.4.* `https://github.com/scikit-optimize/scikit-optimize`.
52. Norris, A. "The isotropic material closest to a given anisotropic material". *Journal of Mechanics of Materials and Structures* **1,** 223–238 (2006).